INTERNATIONAL JOURNAL FOR NUMERICAL METHODS IN FLUIDS
Int. J. Numer. Meth. Fluids **28**: 225–242 (1998)

NUMERICAL AND EXPERIMENTAL INVESTIGATION OF TURBULENT FLOW IN A RECTANGULAR DUCT

MASOUD ROKNI[a], CARL-OLOF OLSSON[b] AND BENGT SUNDÉN[a,*]

[a] *Division of Heat Transfer, Lund Institute of Technology, Box 118, 221 00 Lund, Sweden*
[b] *Department of Thermo and Fluid Dynamics, Chalmers University of Technology, 412 96 Göteborg, Sweden*

SUMMARY

Details of the turbulent flow in a 1:8 aspect ratio rectangular duct at a Reynolds number of approximately 5800 were investigated both numerically and experimentally. The three-dimensional mean velocity field and the normal stresses were measured at a position 50 hydraulic diameters downstream from the inlet using laser doppler velocimetry (LDV). Numerical simulations were carried out for the same flow case assuming fully developed conditions by imposing cyclic boundary conditions in the main flow direction. The numerical approach was based on the finite volume technique with a non-staggered grid arrangement and the SIMPLEC algorithm. Results have been obtained with a linear and a non-linear (Speziale) k–ε model, combined with the Lam–Bremhorst damping functions for low Reynolds numbers. The secondary flow patterns, as well as the magnitude of the main flow and overall parameters predicted by the non-linear k–ε model, show good agreement with the experimental results. However, the simulations provide less anisotropy in the normal stresses than the measurements. Also, the magnitudes of the secondary velocities close to the duct corners are underestimated. © 1998 John Wiley & Sons, Ltd.

KEY WORDS: turbulent flow; non-linear turbulence modelling; secondary flow; rectangular duct

1. INTRODUCTION

Ducts with non-circular cross sections are frequently encountered in industrial heat transfer equipment, e.g. compact heat exchangers, cooling channels in gas turbine blades, nuclear reactors, ventilation and air-conditioning systems, turbomachinery, etc. The main flow in such ducts is influenced by the secondary motions in the plane perpendicular to the streamwise direction, commonly referred to as secondary flows of Prandtl's second-kind. The secondary motions may distort the axial flow and induce a reduction of the volumetric flow rate due to a considerable friction loss, especially in corrugated ducts. These motions are of major concern since they redistribute the turbulence kinetic energy in the cross section of a duct, which in turn affects the heat flux and temperature field distributions.

In order to obtain a reasonable prediction of the flow from numerical simulations, the turbulence model must allow for a secondary flow, which implies that the anisotropy of turbulence has to be modeled fairly correctly. The present investigation includes a comparison between experimental results and numerical calculations of turbulent flow in a straight rectangular duct at a relatively low Reynolds number. The aspect ratio of 1:8 of the cross

* Correspondence to: Division of Heat Transfer, Lund Institute of Technology, Box 118, 221 00 Lund, Sweden.

CCC 0271–2091/98/120225–18$17.50

Received January 1997
Revised June 1997

section and a Reynolds number of 5800 are relevant for flow in heat exchanger ducts, e.g. radiator ducts.

The non-linear $k-\varepsilon$ model proposed by Speziale [1] has been employed for predicting the flow and heat transfer in straight and corrugated ducts with trapezoidal cross sections, see [2,3]. The predicted secondary flows were in agreement with expected flows. However, no quantitative judgement was possible due to the lack of experimental data. Several fundamental investigations concerning turbulent flow in square and rectangular ducts exist. Direct numerical simulations have been performed for a square duct [4,5] and for a plane duct [6] that provide valuable data for evaluation of turbulence models. Large eddy simulations for square ducts are reported by Su and Friedrich [7] at a Reynolds number of 49000 and by Madabhushi and Vanka [8] at a Reynolds number of 5800. Gessner and Jones [9] and Gessner and Emery [10] provided experimental data for square and rectangular ducts for several Reynolds numbers. Numerical calculations for square ducts have also been carried out [2] and the results were in good agreement with reported data. Further discussions on experiments and calculation methods for flow in non-circular ducts involving turbulence-driven secondary motions are found in References [1,11,12].

A linear $k-\varepsilon$ model does not have the ability to predict secondary flows, but it is still one of the most popular models thanks to its simplicity and good overall properties. Adding non-linear terms to the constitutive relation for the Reynolds stresses allows the model to predict anisotropic normal stresses, and then secondary flows may be predicted without solving additional equations. A differential Reynolds stress model (RSM) is able to predict secondary flows; however, the increased complexity of the model may cause stability problems together with a significant increase in computational effort. A non-linear $k-\varepsilon$ model may therefore be an attractive choice for some flow situations. In this investigation, results obtained with a low Reynolds number version of the non-linear $k-\varepsilon$ model of Speziale are compared with experimental data. Also, some results obtained by the linear $k-\varepsilon$ model are presented. The experiments were performed as a reference case in an investigation of the flow in rib-roughened ducts using a LDV technique [13].

In the literature, no numerical investigations have been presented on turbulent flow in a 1:8 aspect ratio rectangular duct. Since the secondary motion and its velocity components are only a few percent of the main flow velocity, measurements of the secondary motion are very difficult. In this work, the numerical calculation is focused on fully developed periodic flow and may be regarded as a further application and evaluation of the computational method developed by Rokni and Sundén [2,3] that has previously been successfully applied in straight and wavy ducts of various cross sections. One purpose is to assess the reliability and accuracy of a non-linear $k-\varepsilon$ model to rectangular ducts of large aspect ratio, which are of interest in compact heat exchangers. Another purpose is to provide numerical and experimental flow characteristics of ducts of interest in engineering applications.

2. PROBLEM STATEMENT

A straight duct with a rectangular cross section is considered in this study. Only one quarter of the duct is considered, by imposing symmetry conditions. A principle sketch of the duct is shown in Figure 1.

The calculation method has been focused on fully developed turbulent flow in a three-dimensional duct.

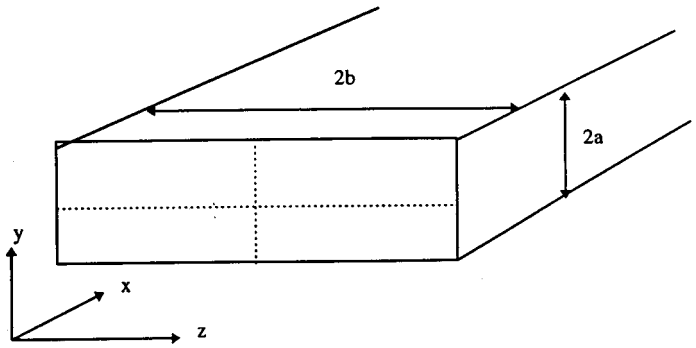

Figure 1. Duct under consideration.

Mean velocity distributions, friction factor, Reynolds stresses and turbulence kinetic energy are determined for fully developed conditions both experimentally and numerically. The Reynolds number is about 5800.

3. EXPERIMENTAL ARRANGEMENT

The flow system for the LDV measurements consists of a fan, a rotameter to measure the flow rate (Krohne, flow range 3–30 $m^3 h^{-1}$), and a by-pass arrangement to control the flow. A seeding unit and a plenum with two turbulence generating grids are placed upstream from the test section and another plenum including a particle filter is placed downstream from the test section, see Figure 2. No smooth contraction is used at the inlet of the rectangular duct. The test section consists of a 56 hydraulic diameters rectangular Plexiglas duct. The height of the

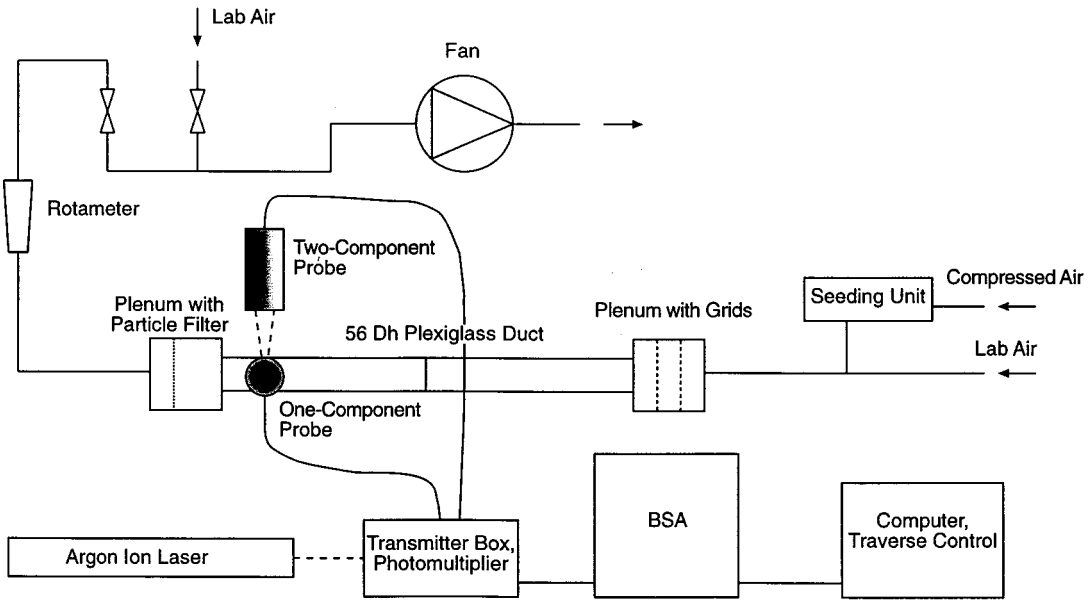

Figure 2. Experimental set-up arrangement.

duct is $2a = 0.0145$ m and the width is $2b = 0.1125$ m. The real aspect ratio is thus $b/a = 7.76$, which is also the value used in the numerical simulations. The measurements were carried out at 50 hydraulic diameters downstream from the inlet.

The flow field velocity was measured using a three-component LDV system with side-scatter arrangement, see Figure 2. However, only one component was used at a time, with a green color of 514.5 nm wavelength. The system was composed of an argon ion laser (COHERENT INNOVA 90), the Dantec fiber-flow series of optical elements, including a transmitter box with a Bragg cell and color separators, a one-component probe and a two-component probe with beam expanders of factor 1.95 and a front lens of 310 mm focal length. The probes contained both transmitting and receiving optics, and the collected light was directed to color separators and further to photomultipliers, where transformation to electric signals was performed. The signals were analyzed in a Dantec burst spectrum analyzer, BSA (57N10), and the position of the probes was controlled using Dantec traverse units 57G20 and 57B100. A computer equipped with BURSTware 3.1 was used to control the LDV hardware and to process the velocity data.

The side-scatter arrangement gives an ellipsoidal measurement volume with approximately 0.05 mm width and 0.10 mm length. The output power of the laser was typically 1.0 W. At each measurement point, 20000 samples were taken. Only validated bursts were stored and used in the evaluation of instantaneous velocities. No corrections for velocity bias were employed. A TSI model 9306 six-jet atomizer was used as the seeding unit with 7% sugar–water solution as the seeding material.

The measurements consisted of 10×14 points and covered one quadrant of the duct cross section plus one row of measurement points on the other side of the lines of symmetry. The points closest to the walls were 0.5 mm ($y^+ \approx 8$) from the short wall and 1.25 mm ($y^+ \approx 19$) from the wide wall.

3.1. Estimation of uncertainty

The uncertainty in the presented experimental velocity data is related to the uncertainty of the duct geometry and the uncertainties connected with the LDV technique. The dimensions of the Plexiglas duct are accurate to within ± 0.1 mm. The major source of errors is the orientation of the probes and the positioning of the measurement volume with respect to the duct. The adjustment of the probe orientation has been performed through measuring the V- and W-velocity components on the centerline and turning the probes until these components are < 0.005 m s^{-1}, which is the estimated resolution in velocity due to the statistical uncertainty at this position. The U-component, which is of the order of 1 m s^{-1}, has thus an uncertainty of $\pm 0.5\%$. The V- and W-components are of the order of 0.05 m s^{-1} close to the corners, while they are < 0.01 m s^{-1} in the rest of the duct and may thus, have an uncertainty greater than $\pm 10\%$ in magnitude. Evidently, the direction of the secondary flow will suffer a large uncertainty. The position of the measurement volume has been related to the duct co-ordinate system through finding a corner of the duct by analyzing the signals from the photomultipliers, and the uncertainties are estimated to be within ± 0.05 mm in both the y- and z-directions. Assuming a Gaussian distribution and taking the root mean square (rms) value as an estimate of the true standard deviation, the statistical uncertainty in the velocity measurements is given as $\Delta U = \pm 1.96 U\text{rms}/\sqrt{N}$ with 95% confidence, where N is the number of samples. In the worst case of a turbulent flow with $U\text{rms} = 0.5$ m s^{-1} and $N = 20000$, the uncertainty is ± 0.007 m s^{-1}, which in the wall regions would correspond to an uncertainty less than $\pm 0.7\%$ in the U-component. The error due to the signal processing in the BSA is negligible with the settings being used.

4. NUMERICAL PROCEDURE

The governing equations are the continuity and momentum equations. Fully developed periodic turbulent flow is considered in this investigation. The following assumptions are employed: steady state, no-slip at the walls and constant fluid properties. One then has

$$\frac{\partial}{\partial x_j}(\rho U_j) = 0, \tag{1}$$

$$\frac{\partial}{\partial x_j}(\rho U_i U_j) = -\frac{\partial P}{\partial x_i} + \frac{\partial}{\partial x_j}\left[\mu\left(\frac{\partial U_i}{\partial x_j} + \frac{\partial U_j}{\partial x_i}\right)\right] + \frac{\partial}{\partial x_j}(-\rho\overline{u_i u_j}). \tag{2}$$

The Reynolds stresses $(-\rho\overline{u_i u_j})$ are modeled as described in the following section.

4.1. Turbulence model for stresses

The most widely used two-equation turbulence model, the so-called k–ε model is also used here. This model is combined with damping functions to increase the accuracy near the walls. The conventional low Reynolds number k–ε model [14] for steady state is given by

$$\frac{\partial}{\partial x_j}(\rho U_j k) = \frac{\partial}{\partial x_j}\left[\left(\mu + \frac{\mu_\tau}{\sigma_k}\right)\frac{\partial k}{\partial x_j}\right] + P_k - \rho\varepsilon, \tag{3}$$

$$\frac{\partial}{\partial x_j}(\rho U_j \varepsilon) = \frac{\partial}{\partial x_j}\left[\left(\mu + \frac{\mu_\tau}{\sigma_\varepsilon}\right)\frac{\partial \varepsilon}{\partial x_j}\right] + f_1 C_{\varepsilon 1}\frac{\varepsilon}{k}P_k - f_2 C_{\varepsilon 2}\rho\frac{\varepsilon^2}{k}, \tag{4}$$

where P_k is the production term expressed as

$$P_k = \tau_{ij}\frac{\partial U_i}{\partial x_j} = -\rho\overline{u_i u_j}\frac{\partial U_i}{\partial x_j}, \tag{5}$$

and f_1 and f_2 are damping functions.

The turbulent eddy viscosity μ_τ is calculated as

$$\mu_\tau = \rho f_\mu C_\mu \frac{k^2}{\varepsilon}, \tag{6}$$

where f_μ is the damping function for the turbulent viscosity.

In the linear eddy viscosity model, the Reynolds stresses τ_{ij} are expressed as

$$\tau_{ij} = -\frac{2}{3}\rho k\delta_{ij} + 2\mu_\tau S_{ij}. \tag{7}$$

A non-linear constitutive relationship for the Reynolds stresses in incompressible flow was proposed by Speziale [1]. The non-linear terms in this model are a form of quadratic terms which enable calculation of anisotropic normal stresses and consequently prediction of the secondary velocity field in ducts. The Reynolds stresses in this model are determined according to

$$\tau_{ij} = -\frac{2}{3}\rho k\delta_{ij} + 2\mu_\tau S_{ij} + 4C_{\mathrm{D}}C_\mu\mu_\tau\frac{k}{\varepsilon}\left(S_{ik}S_{kj} - \frac{1}{3}S_{mn}S_{nm}\delta_{ij}\right) + 4C_{\mathrm{E}}C_\mu\mu_\tau\frac{k}{\varepsilon}\left(\dot{S}_{ij} - \frac{1}{3}\dot{S}_{mm}\delta_{ij}\right), \tag{8}$$

where

$$S_{ij} = \frac{1}{2}\left(\frac{\partial U_i}{\partial x_j} + \frac{\partial U_j}{\partial x_i}\right), \tag{9}$$

and $\dot{S}_{ij}$ is the frame-indifferent Oldroyd derivative (see [14]) of S_{ij} in the form of

$$\dot{S}_{ij} = \frac{\partial S_{ij}}{\partial t} + U_k \frac{\partial S_{ij}}{\partial x_k} - \frac{\partial U_i}{\partial x_k} S_{kj} - \frac{\partial U_j}{\partial x_k} S_{ki}. \tag{10}$$

In Equation (10), the time derivative is zero since a steady state condition is considered.

The standard values for the constants and coefficients in Equations (3), (4), (6) and (8) have been used as shown below,

σ_k	σ_ε	$C_{\varepsilon 1}$	$C_{\varepsilon 2}$	C_D	C_E	C_μ
1.0	1.314	1.44	1.92	1.68	1.68	0.09

4.2. The damping functions f_1, f_2 and f_μ

The high Reynolds number form of the k–ε model suggests that f_μ should be approximately equal to unity in the fully turbulent region remote from solid walls. However, in a region very close to a wall where the viscous effects become very important, f_μ will differ considerably from unity. In this study, the Lam–Bremhorst [15] formulations of f_1, f_2 and f_μ are used. f_μ is determined as

$$f_\mu = (1 - e^{-0.0165 Re_k})^2 \left(1 + \frac{20.5}{Re_t}\right), \tag{11}$$

where

$$Re_k = \frac{\rho k^{0.5} \eta}{\mu} \quad \text{and} \quad Re_t = \frac{\rho k^2}{\mu \varepsilon}.$$

f_1 and f_2 are calculated as

$$f_1 = 1 + \left(\frac{0.05}{f_\mu}\right)^3, \tag{12}$$

and

$$f_2 = 1 - e^{-Re_t^2}. \tag{13}$$

4.3. Periodic condition

Periodic means that the flow varies in a cyclic manner along the main flow direction at large downstream distances. In other words, the velocity profile repeats itself successively in the fully developed region. There is no need to calculate the developing region if only the fully developed region is of interest. The computational time and cost decrease significantly by applying a reasonable periodic condition to the velocity components, since the number of grid points in the main flow direction can be decreased considerably. The idea of using periodic conditions for the calculation of the fully developed region was initiated by Patankar *et al.* [16], originally for corrugated surfaces. It has now been used by several authors, e.g. Rokni

and Sundén [2,3]; Prata and Sparrow [17]; Faghri and Asako [18]; Webb and Ramadhyani [19], and others.

It is obvious that the pressure P decreases in the main flow direction and therefore, the pressure should be handled in a special way. It is expressed as

$$P(x, y, z) = -\beta x + P^*(x, y, z), \tag{14}$$

where β is a constant representing the non-periodic pressure gradient and is related to the global mass flow. P^* behaves in a periodic manner from cycle-to-cycle in the flow direction. Inserting Equation (14) into the momentum equation (2) gives

$$\frac{\partial}{\partial x_j}(\rho U_i U_j) = \beta \frac{\partial x}{\partial x_i} - \frac{\partial P^*}{\partial x_i} + \frac{\partial}{\partial x_j}\left[\mu\left(\frac{\partial U_i}{\partial x_j} + \frac{\partial U_j}{\partial x_i}\right)\right] + \frac{\partial}{\partial x_j}(-\rho\overline{u_i u_j}), \tag{15}$$

where $\partial x/\partial x_i$ is equal to unity in the x-direction (U-velocity) and zero in the y- and z-directions (V- and W-velocities).

4.4. Boundary conditions

Periodicity conditions are imposed at the inlet and outlet for all variables. It then follows

$$\Phi(x, y, z) = \Phi(x + L, y, z) \quad \Phi = U, V, W, P^*, k, \varepsilon. \tag{16}$$

In order to achieve stability in the numerical procedure, the following variables are also handled as periodic

$$\overline{u_i u_j}, S_{ij}, f_\mu.$$

The boundary conditions $k = \partial\varepsilon/\partial\eta = 0$ at the walls and $\partial k/\partial\eta = \partial\varepsilon/\partial\eta = 0$ at the symmetry lines are adopted in this study. η is a normal distance to a wall or a symmetry line. The effect of one wall, namely the nearest one, is adopted in this investigation, $\eta = \min(\eta_1, \eta_2)$.

4.5. Additional equations

The Reynolds number is defined as

$$Re = \frac{\rho U_b D_h}{\mu} = \frac{\dot{m} D_h}{A_{cross}\mu}, \tag{17}$$

where A_{cross} is the cross sectional area and U_b is the bulk velocity which is related to the mass flow as

$$\dot{m} = \int_A \rho U \, dA. \tag{18}$$

The pressure drop per cycle is defined by

$$\Delta p = \beta L = f\frac{L}{D_h}\frac{\rho U_b^2}{2}, \tag{19}$$

where f is the Darcy friction factor. One then has

$$f = \frac{\beta D_h}{\rho U_b^2/2}. \tag{20}$$

The calculated friction coefficient is compared with the Petukhov friction factor [20], which is valid for $3000 \le Re \le 5 \times 10^6$.

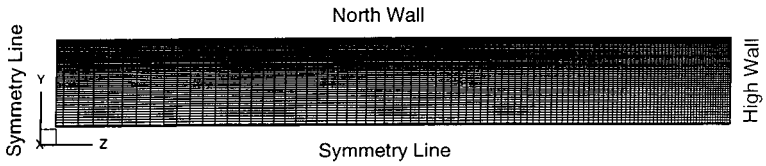

Figure 3. Grid distribution, 51×101 grid points.

$$C_f = \frac{f}{4} = (0.790 \ln Re - 1.64)^{-2}/4. \tag{21}$$

4.6. Numerical solution procedure

The partial differential equations are transformed to algebraic equations by a general finite volume technique. The momentum equations are solved for the velocity components on a non-staggered grid arrangement. The Rhie–Chow interpolation method [21] is used to interpolate the velocity components to the control volume faces from the grid points. The SIMPLEC algorithm [22] is employed to handle the pressure velocity coupling. TDMA (see, e.g. [23]) based algorithms are used for solving the equations. The convective terms are treated by the hybrid [23] and van Leer [24] schemes, while the diffusive terms are treated by the central difference scheme. The results of using the hybrid and van Leer schemes were almost identical.

The numerical procedure is based on solving the general equation

$$\frac{\partial}{\partial t}(\rho\Phi) + \frac{\partial}{\partial x_j}(\rho\Phi U_j) = \frac{\partial}{\partial x_j}\left[\Gamma_\Phi \frac{\partial \Phi}{\partial x_j}\right] + S_\Phi. \tag{22}$$

A non-uniform grid distribution is employed in the plane perpendicular to the main flow direction. Close to each wall, the number of grid points or control volumes is increased to enhance the resolution and accuracy. Figure 3 shows a typical distribution of grid points.

The dynamic viscosity was set to 18.1×10^{-6} Pa s and the density was set to 1.189 kg m^{-3}. The initial values for all variables are set to zero except for k and ε. These are set as

$$k = 0.005 U_{\text{in}}^2 \qquad \varepsilon = 0.1 k^2.$$

The initial values for k and ε are very important in periodic conditions. If U_{in} is too low, k and ε are not activated, while a too high value of U_{in} causes divergence problems. The interval within which U_{in} may be varied is very narrow. This property seems to impose a limitation of using existing damping functions (presented in the literature) for periodic conditions.

The computations were terminated when the sum of the absolute residuals normalized by the inflow was less than 2×10^{-4} for all variables. Different numbers of grid points were used in the cross sectional plane, namely 26×42, 31×51 and 51×101. Only three grid points were applied in the main flow direction. The overall friction factors, which are most interesting from an engineering point of view, did not change significantly if the number of grid points was increased beyond 31×51. However, local values of the Reynolds stresses are somewhat depending on the number and distribution of the grid points. The results are presented for 51×101 grid points.

It is important to make sure that some grid points near the walls are in the viscous sublayer and perhaps the mean values of y^+ at the first grid points adjacent to each wall should be of order unity.

5. RESULTS AND DISCUSSION

5.1. Overall properties

The predicted secondary velocity vectors using the non-linear k–ε model are shown in Figure 4. The secondary motions consist of two counter rotating vortices that transport high momentum fluid towards the duct corner and then outwards along the walls. The vortices meet along the symmetry line $y = 0$ at $z/b \approx 0.92$. It is obvious that the sizes of the vortices are different and strong inhomogeneities exist between them. Close to the short symmetry line ($z/b = 0$) the secondary flow has a very small magnitude and it may be expected that it has no influence on the streamwise flow, hence the flow properties along this line can be expected to be similar to those obtained in a parallel plane duct. There is an overall agreement between the numerical and experimental results, although the latter ones are only available at relatively few positions.

Figure 5 shows the streamwise velocity contours predicted by the non-linear k–ε model together with the LDV measurements. The experiment shows that in the region close to the corner, the contours are bulged towards the corner due to the presence of secondary motions. The non-linear k–ε model shows a slightly bulging behavior towards the corner. Again, since the experimental data are available at fewer positions, the contours of the experimental axial velocity are not smooth.

Overall experimental results and the predicted mean values agree very well. The Reynolds numbers for the simulations with the linear and non-linear models are 5920 and 5860, respectively, which are close to the Reynolds number $Re \approx 5800$ in the experiment. The

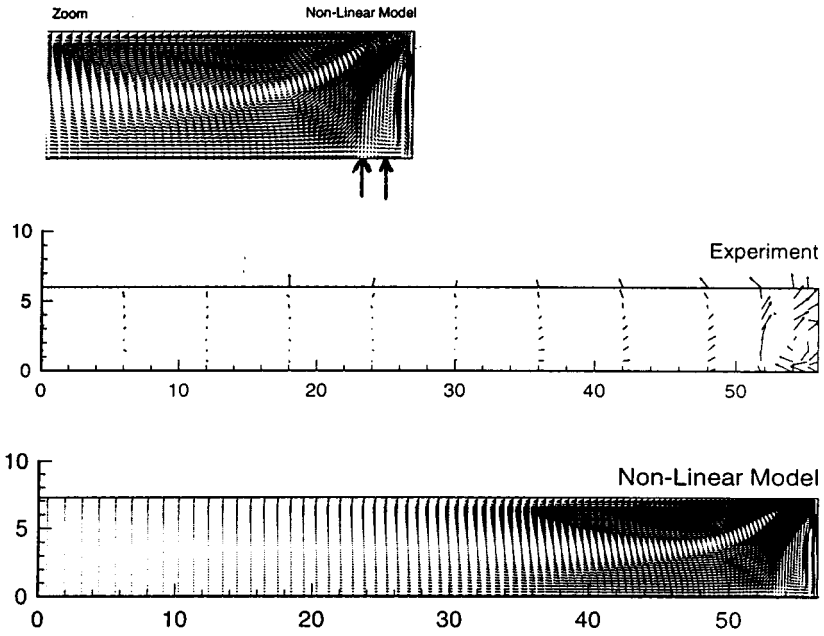

Figure 4. Predicted and measured secondary velocities. Note that the upper boundary line for the experiment is through the first measured points from the wall. For the sake of clarity part of the predicted secondary motion has been zoomed. Please note that only the upper right hand quadrant of the cross section is shown. The two arrows show the positions where the numerical results and the experimental measurements are compared in details. Dimensions are in mm.

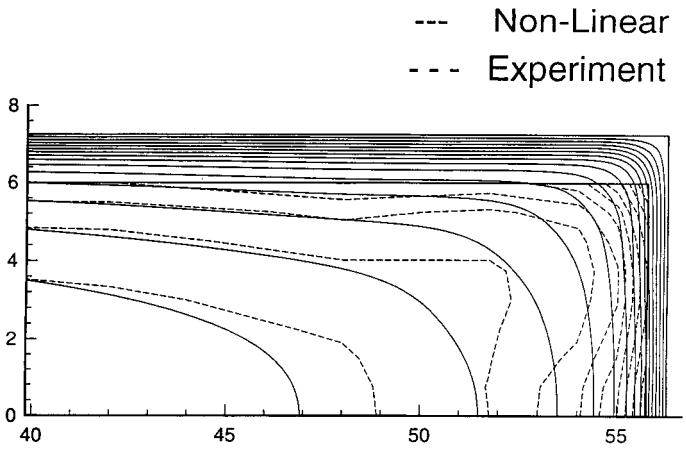

Figure 5. Predicted and measured main flow contours.

computed skin friction coeffficient, $C_f = \tau_w/(0.5\rho U_b^2)$ is 9.41×10^{-3} for the non-linear and 9.23×10^{-3} for the linear model. These values agree very well with the Petukhov correlation (Equation (21)) 9.20×10^{-3} and 9.17×10^{-3}, respectively. Other calculated mean properties are presented in Table I. These results are very close to the DNS data for a parallel plane duct at $Re \approx 5600$ presented by Kim *et al.* [6].

In Table I, and later in following figures, the friction velocity for each simulation is estimated from the mean values of friction velocities at the grid points adjacent to the walls.

5.2. Position $z/b = 0$ (symmetry line)

The streamwise velocity profile along the symmetry line is presented in Figure 6. It is found

Table I. Mean flow properties predicted by non-linear and linear k-ε models.

Non-Linear	Linear
$Re = \dfrac{\rho U_b D_h}{\mu} \approx 5860$	$Re = \dfrac{\rho U_b D_h}{\mu} \approx 5920$
$Re_c = \dfrac{\rho U_c D_h}{2\mu} \approx 3660$	$Re_c = \dfrac{\rho U_c D_h}{2\mu} \approx 3700$
$Re_\tau = \dfrac{\rho u_\tau D_h}{2\mu} \approx 200$	$Re_\tau = \dfrac{\rho u_\tau D_h}{2\mu} \approx 200$
$\dfrac{U_b}{u_\tau} = 14.63$	$\dfrac{U_b}{u_\tau} = 14.81$
$\dfrac{U_c}{U_b} = 1.25$	$\dfrac{U_c}{U_b} = 1.25$
$\dfrac{U_c}{u_\tau} = 18.30$	$\dfrac{U_c}{u_\tau} = 18.53$
$C_f = \dfrac{\tau_w}{0.5\rho U_b^2} = 9.41 \times 10^{-3}$	$C_f = \dfrac{\tau_w}{0.5\rho U_b^2} = 9.23 \times 10^{-3}$
$C_{f0} = \dfrac{\tau_w}{0.5\rho U_c^2} = 6.03 \times 10^{-3}$	$C_{f0} = \dfrac{\tau_w}{0.5\rho U_c^2} = 5.90 \times 10^{-3}$

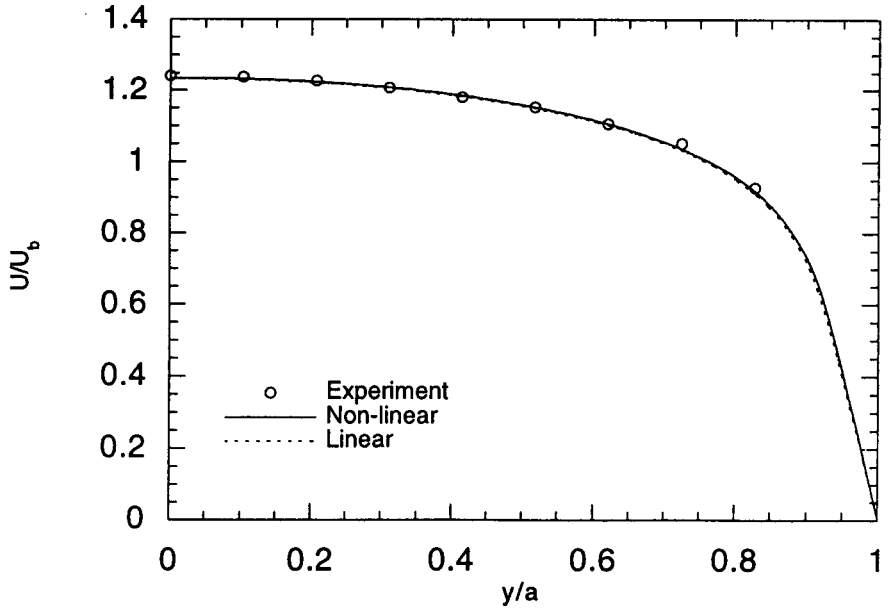

Figure 6. Main flow velocity at the centerline.

that the predicted results agree very well with the experimental data. The center-to-bulk velocity ratio (U_c/U_b), is 1.25 in the non-linear k–ε model as well as in the linear k–ε model, but 1.23 in the experiment. This ratio can be compared with the correlation $U_c/U_b = 1.28Re_m^{-0.0116}$ for parallel plane ducts according to Dean [25]. This correlation gives 1.16 if the hydraulic diameter is used as reference length. Gavrilakis [5] obtained the value of 1.33 for a square duct at the Reynolds number 4410 from direct numerical simulations. Demuren and Rodi [11] showed that the ratio U_c/U_b slightly decreases with increasing Reynolds number, and they established a value close to 1.25 at a Reynolds number of about 25000 in a square duct.

The centerline velocity-to-friction velocity ratio (U_c/U_τ) is calculated to be 18.22, which is very close to the value of 18.20, reported by Kim *et al.* [6] for a plane duct. The friction coefficient based on centerline velocity calculated by the non-linear model is 6.02×10^{-3}, which is in excellent agreement with the value 6.04×10^{-3} obtained by Kim *et al.* [6].

Turbulence intensities normalized by the friction velocity u_τ are shown in Figure 7. The u' values ($\sqrt{\bar{u}\bar{u}}/u_\tau$) predicted by the non-linear k–ε model are consistent with the experimental data close to the centerline while the peak value close to the wall is somewhat underestimated. However, the non-linear model predicts isotropy at the centerline, whereas the experimental data show anisotropy at this line. Isotropy prediction by the non-linear model at the centerline may be called '*return to isotropy at the duct's center*' and from a mathematical point of view the *return to isotropy at the duct's center* is obvious (see Equation (8)) since the Reynolds stresses, predicted by the non-linear model, depend on the mean velocity gradients. Most of these are zero at the duct's center since symmetry and fully developed conditions are assumed. Those velocity gradients not being exactly zero can be shown to be very small at low Reynolds numbers. However, at sufficiently high Reynolds numbers this will not necessarily be true. The non-linear model overestimates the v' and w' components (in order to achieve *return to isotropy at the duct's center*), but the trend in the curves are similar to that in the experimental data. The difference between v' and w' ($v' - w'$) is in excellent agreement with the experiment.

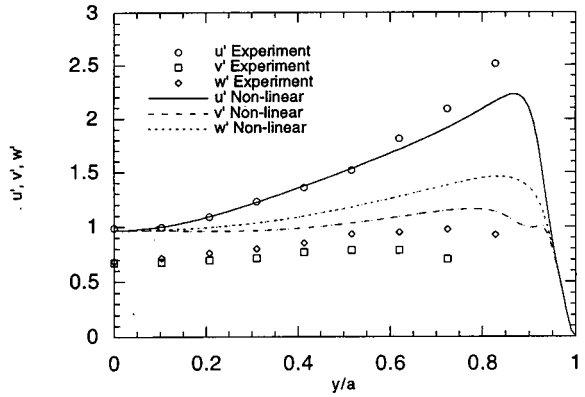

Figure 7. Predicted and measured turbulent normal intensities at the centerline.

In the present experiment, u' attains a value close to 1.0 at the centerline, while v' and w' have values close to 0.7. The corresponding values in plane duct flow are 0.8 and 0.6, respectively, as reported by Kim *et al.* [6], and in a square duct the values are 1.2 and 0.7, respectively, according to Huser and Biringen [4] at $Re \approx 10320$. If the Reynolds number difference between the above mentioned investigations is ignored, it can be concluded that the anisotropy is increased as the duct geometry approaches a square duct. The component normal to the wall, v', was not measured as close to the wall as the other components due to limited access of the laser beams.

Since the normal intensities v' and w' are overestimated by the non-linear model, the predicted kinetic energies are also higher than in the experiment, see Figure 8. The non-linear model predicts higher values than the linear model but the distributions are similar in form.

5.3. Position $z/b = 0.92$

In order to compare the predicted results with experiments at a crucial position, the position $z/b = 0.92$ was chosen. The two vortices meet each other at this position on the symmetry line $y/a = 0$. Figures 9–12 show these comparisons.

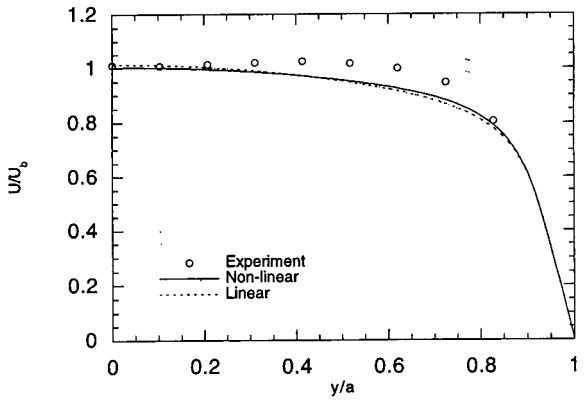

Figure 8. Predicted and measured turbulent kinetic energy at the centerline.

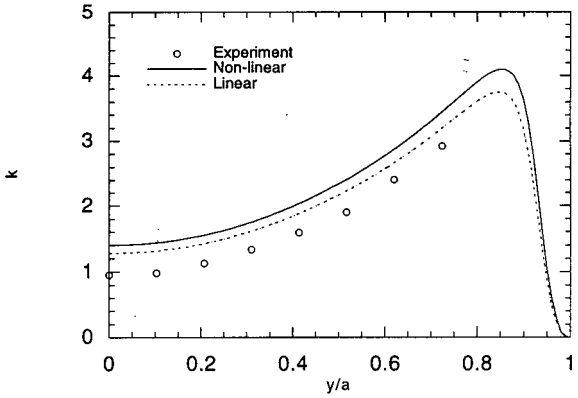

Figure 9. Main flow velocity at position $z/b = 0.92$.

Both the linear and non-linear models predict the streamwise velocity in agreement with the experiment as can be seen in Figure 9. However, the experimental data indicate a larger influence of the secondary velocity and a slight bulging of the curve towards the corner occurs.

The measured and simulated V- and W-velocity components are shown in Figures 10 and 11. According to the symmetry condition at $y/a = 0$, the V-component must be equal to zero along this line but, as seen in Figure 10, the measured V-velocity is not equal to zero. As discussed previously, the uncertainty in the V- and W-components in the measurements is high and since these components are very small in magnitude it is difficult to maintain accuracy at all positions. However, it might be so that some geometry defect is present in the experimental set-up and as an effect, an unsymmetric distribution of V-velocity occurs. If the measured V-value at $y/a = 0$ is subtracted from all the measured V-values, then the predicted and measured V-values are in good agreement. The measured V-velocity at $y/a = 0.51$ seems to be unrealistic. The general trend is similar in the experiment and predictions.

The W-velocity shown in Figure 11 is negative close to the wall, where the flow is directed away from the corner (in the large vortex). At approximately $y/a = 0.7$, the W-velocity changes sign since the flow in this region is directed towards the corner. Hence, in the measurement, the small vortex seems to extend from the short wall as far out as $z/b = 0.92$, while the simulations show that this position belongs to the larger vortex.

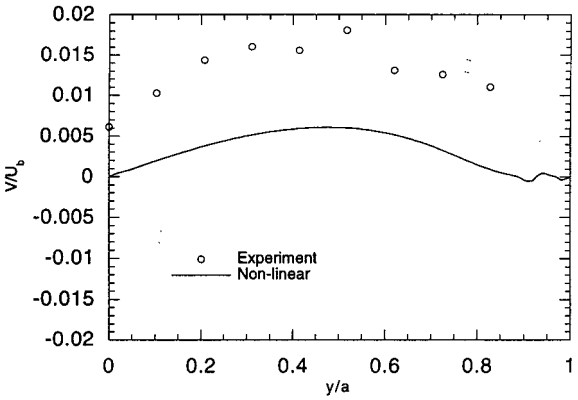

Figure 10. Measured and predicted V-velocity normalized by bulk velocity at $z/b = 0.92$.

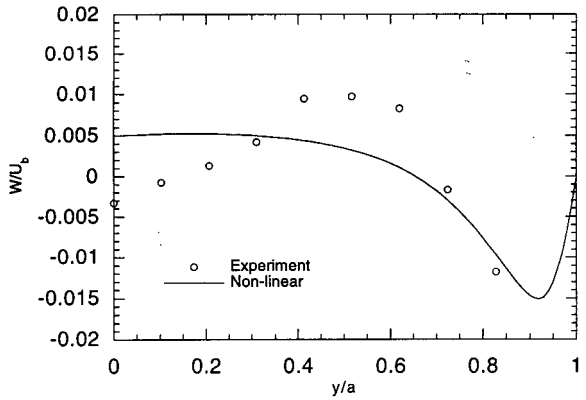

Figure 11. Measured and predicted W-velocity normalized by bulk velocity at $z/b = 0.92$.

The linear eddy viscosity model does not predict any secondary motion and thereby the mean V and W-velocities are zero.

The turbulence intensities are shown in Figure 12. The u' turbulence intensity reaches the value of about 1.4 at the symmetry line $y/a = 0$, in both the experiment and the non-linear model simulation. The predicted peak value for the u' turbulence intensity is also in good agreement with the experimental value. The overestimation of v' and w' intensities, because of *return to isotropy at the duct's center*, are similar to those discussed for $z/b = 0$ in Figure 7. The experiment shows that $v' - w'$ changes sign at $y/a \approx 0.5$, which is captured very well by the simulation. The anisotropy at the symmetry line and for all y/a is also well captured by the numerical simulation.

5.4. Position $z/b = 0.96$ (near the short wall)

Another position of interest in comparing experimental data and predictions may be $z/b = 0.96$. This position is very close to the center of the small vortex (about 0.03 mm to the west of the center, the average z^+ is about 35 in this position). Figures 13–16 show U-, V- and W-velocity components as well as the turbulence intensities at this position, respectively. For the U-velocity shown in Figure 13, the differences between the results obtained from the

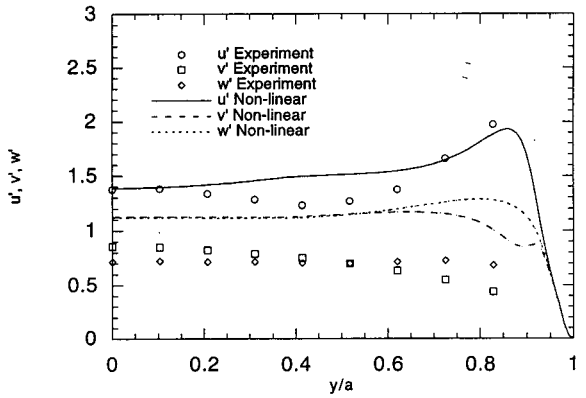

Figure 12. Predicted and measured turbulent normal intensities at $z/b = 0.92$.

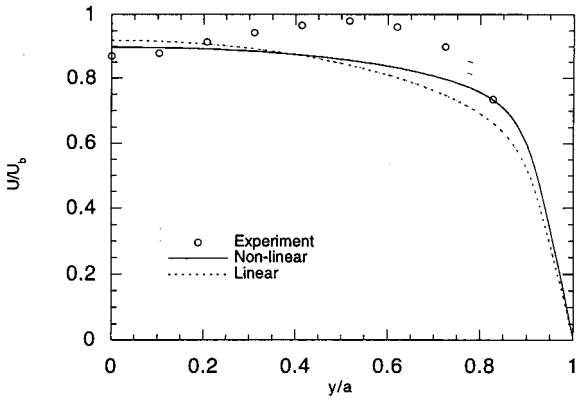

Figure 13. Main flow velocity at position $z/b = 0.96$.

non-linear model and the linear model are clear. The secondary motion predicted by the non-linear model influences the main flow velocity (bulge it towards the corner) but not as much as the experiments indicate. The differences between experiments and predictions are greater than at $z/b = 0.92$.

The V-velocity in Figure 14 is positive for all y/a, which indicates that the center of the small vortex is closer to the short wall than $z/b = 0.96$, see also Figure 4. Again the experiments do not show zero V-velocity at the symmetry line $y/a = 0$, which may partly be related to the uncertainty of the experimental data. However, as pointed out previously, some geometry defect in the experimental set-up may be present and causing a non-zero V-value at $y/a = 0$. Near the wall $y/a = 1$, the V-component must decrease and be zero at the wall. The simulations clearly show this phenomenon but the experiments do not indicate such a trend. However, it should be noted that the experiments only continue to $y/a \approx 0.8$.

It is very important to mention that even if the experiment shows asymmetry near the symmetry line, the simulations can never predict it, since the problem is always idealized (even a very sophisticated turbulence model, such as the differential Reynolds stress model can not show the asymmetry near a symmetry line). The asymmetry found in the experiment may be due to some uncontrolled disturbance that could not be discovered.

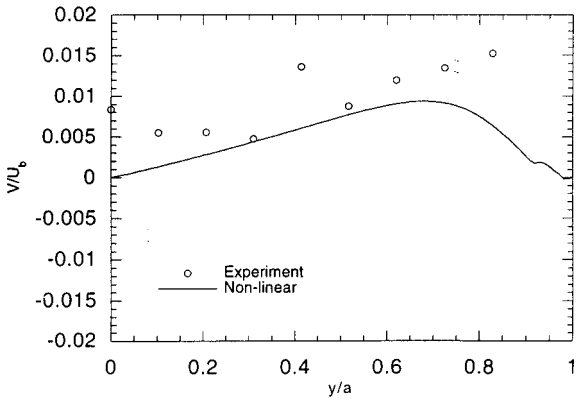

Figure 14. Measured and predicted V-velocity normalized by bulk velocity at $z/b = 0.96$.

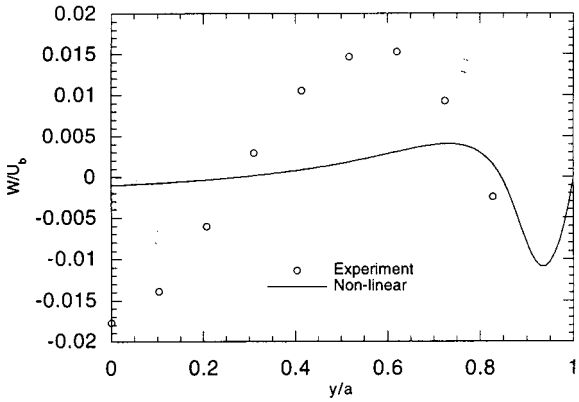

Figure 15. Measured and predicted W-velocity normalized by bulk velocity at $z/b = 0.96$.

The W-velocity changes sign at approximately the same position ($y/a \approx 0.77$) in both the measurement and the simulations, see Figure 15. However, in general, the magnitude is much smaller in the simulations than in the measurements. The experiment also shows relatively large negative values of W at positions of $y/a < 0.3$, while the simulations present only modest negative values. This can explain, that in the experiment, the rotation of the small vortex near its center is much larger than in the predictions (modest rotation by simulations). This phenomenon will affect the normal intensities as seen in Figure 16.

The measured u' has a maximum at $y/a = 0$. It then decreases and passes a minimum at $y/a \approx 0.6$ and then starts to increase again. The predictions also show a maximum at $y/a = 0$, but then a very modest decrease at larger y/a until the wall region is reached. Then u' rapidly approaches zero. It can be noted that, even though the v' and w' intensities are overestimated in the simulations (because of *return to isotropy at the duct's center*), the differences between these intensities are in good agreement with the experimental data. At a certain position, w' becomes greater than v'. In the experiments, this position is at $y/a \approx 0.70$, while in the simulations it is at $y/a \approx 0.75$. Thus this occurrence is rather well captured.

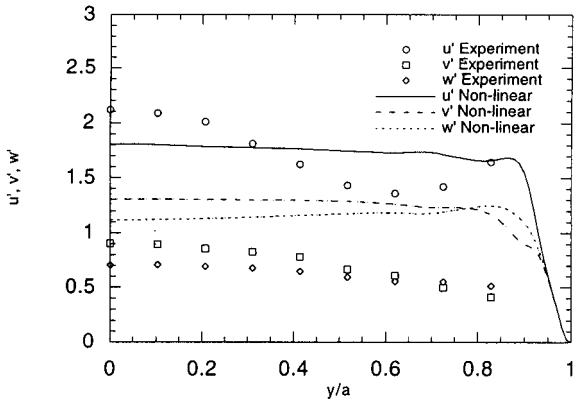

Figure 16. Predicted and measured turbulent normal intensities at $z/b = 0.96$.

6. CONCLUSIONS

A numerical and experimental investigation of turbulent flow in a straight duct with a 1:8 aspect ratio has been presented. Speziale's non-linear eddy viscosity model was successfully used to predict the secondary velocity field, the streamwise velocity and the friction factor. Comparisons with results obtained with the linear eddy viscosity model were also presented. Numerical and experimental results of the flow characteristics have been compared at two crucial positions, namely near the center of the small vortex (close to the shorter wall) and at a position where the two vortices meet and change directions. Comparisons between the numerical and experimental results are also presented at the short symmetry line.

The average friction factor predicted with both models agrees very well with the Petukhov correlation. This might be surprising, but in this flow situation, the influence of the secondary flow on the friction factor is small and an accurate prediction of the secondary flow is not necessary. The influence of the secondary velocities in wavy ducts might be more important and thus the linear model may not be able to provide acceptable results, while the non-linear model may. The velocity distribution along the short symmetry line is in excellent agreement with the experimental data.

The predicted secondary flow patterns using the non-linear model are in good qualitative agreement with the experimental secondary flow patterns. The predicted streamwise velocity profile, as well as the u' intensity, agree very well with experimental data. However, there exist some discrepancies between the computed v' and w' intensities and the experimental results, which are discussed and related (or influenced) to the *return to isotropy at the duct's center*. Also, the *return to isotropy at the duct's center*, might be a reason why the turbulence intensities are overestimated by the non-linear model. The difference between v' and w' $(v' - w')$ is however, captured very well by the non-linear model.

A disadvantage of any non-linear model at low Reynolds number and fully developed duct flow has been identified and defined as *return to isotropy at the duct's center*. This phenomenon can not be overcome if a non-linear k–ε model is used. The reason is that such a model (any non-linear k–ε model) depends on the velocity gradients at the duct's center and for fully developed flow, these gradients become zero or close to zero. The problem may be overcome by, e.g. a differential Reynolds stress model (RSM), but to the expense of a significant increase in computational time and effort, which may not be suitable in general 3D channels.

REFERENCES

1. C.G. Speziale, 'On non-linear k–l and k–ε models of turbulence', *J. Fluid Mech.*, **178**, 459–475 (1987).
2. M. Rokni and B. Sundén, 'A numerical investigation of turbulent forced convection in ducts with rectangular and trapezoidal cross section area by using different turbulence models', *Numer. Heat Transf.*, **30**, 321–346 (1996).
3. M. Rokni and B. Sundén, '3D numerical investigation of turbulent forced convection in wavy ducts with trapezoidal cross section', *Numer. Methods Heat Fluid Flow*, **8**, 118–141 (1998).
4. A. Huser and S. Biringen, 'Direct numerical simulation of turbulent flow in a square duct', *J. Fluid Mech.*, **257**, 65–95 (1993).
5. S. Gavrilakis, 'Numerical simulation of low Reynolds number turbulent flow through a straight square duct', *J. Fluid Mech.*, **244**, 101–129 (1992).
6. J. Kim, P. Moin and R. Moser, 'Turbulence statistics in fully developed channel flow at low Reynolds number', *J. Fluid Mech.*, **177**, 133–166 (1987).
7. M.D. Su and R. Friedrich, 'Investigation of fully developed turbulent flow in a straight duct with large eddy simulation', *J. Fluid Eng.*, **116**, 677–684 (1994).
8. R.K. Madabhushi and S.P. Vanka, 'Large eddy simulation of turbulence-driven secondary flow in a square duct', *Phys. Fluid A*, **3**, 2734–2745 (1991).
9. F.B. Gessner and J.B. Jones, 'On some aspects of fully developed turbulent flow in rectangular channels', *J. Fluid Mech.*, **23**, 689–713 (1965).

10. F.B. Gessner and A.F. Emery, 'The numerical prediction of developing turbulent flow in rectangular ducts', *ASME J. Fluid Eng.*, **103**, 445–455 (1981).
11. A.O. Demuren and W. Rodi, 'Calculation of turbulence driven secondary motion in non-circular ducts', *J. Fluid Mech.*, **140**, 189–222 (1984).
12. A.O. Demuren, 'Calculation of turbulence driven secondary motion in ducts with arbitrary cross section', *AIAA J.*, **29**, 531–537 (1990).
13. C.O. Olsson and B. Sunden, 'Experimental study of flow and heat transfer in rib-roughened rectangular channels', *Exp. Therm. Fluid Sci.* (1998) in press.
14. D.C. Wilcox, 'Turbulence modeling for CFD', *ISBN 0-9636051-0-0*, DCW Industries, USA, 1993.
15. C.K.G. Lam and K. Bremhorst, 'A modified form of the $k-\varepsilon$ model for predicting wall turbulence', *ASME J. Fluid Eng.*, **103**, 456–460 (1981).
16. S.V. Patankar, C.H. Liu and E.M. Sparrow, 'Fully developed flow and heat transfer in ducts having streamwise periodic variations of cross sectional area', *ASME J. Heat Transf.*, **99**, 180–186 (1977).
17. A.T. Prata and E.M. Sparrow, 'Heat transfer and fluid flow characteristics for an annulus of periodically varying cross section', *Numer. Heat Transf.*, **7**, 285–304 (1984).
18. M. Faghri and Y. Asako, 'Numerical determination of heat transfer and pressure drop characteristics for converging–diverging flow channel', *ASME Winter Ann. Meet.*, *Paper 84-WA-HT-12*, 1984.
19. B.W. Webb and S. Ramadhyani, 'Conjugate heat transfer in a channel with staggered ribs', *Int. J: Heat Mass Transf.*, **28**, 1679–1687 (1985).
20. F.P. Incropera and D.P. DeWitt, *Fundamentals of Heat and Mass Transfer*, 4th edn, Wiley, New York, 1996.
21. C.M. Rhie and W.L. Chow, 'Numerical study of the turbulent flow past an airfoil with trailing edge separation', *AIAA J.*, **21**, 1525–1532 (1983).
22. G.D. Raithby and G.E. Schneider, 'Elliptic systems: finite difference method II', in W.J. Minkowycz, E.M. Sparrow, G.E. Schneider, R.H. Pletcher (eds), *Handbook of Numerical Heat Transfer*, Ch 7, Wiley, New York, 1988.
23. S.V. Patankar, *Numerical Heat Transfer and Fluid Flow*, McGraw-Hill, New York, 1980.
24. B. van Leer, 'Towards the ultimate conservative difference scheme, II. Monotonicity and conservation combined in a second-order scheme', *J. Comp. Phys.*, **14**, 361–370 (1974).
25. Dean, R.B., 'Reynolds number dependence of skin friction and other bulk flow variables in two-dimensional rectangular duct flow', *ASME J. Fluid Eng.*, **100**, 215–223 (1978).

